Evolution of Polytypism in GaAs Nanowires during Growth Revealed by Time-Resolved *in situ* x-ray Diffraction

Philipp Schroth, Martin Köhl, and Jean-Wolfgang Hornung

Institute for Photon Science and Synchrotron Radiation, Karlsruhe Institute of Technology,
Hermann-von-Helmholtz-Platz 1, 76344 Eggenstein-Leopoldshafen, Germany

Emmanouil Dimakis

Paul-Drude-Institut für Festkörperelektronik, Hausvogteiplatz 5-7, 10117 Berlin, Germany and Helmholtz-Zentrum
Dresden-Rossendorf, Bautzner Landstraße 400, 01328 Dresden, Germany

Claudio Somaschini and Lutz Geelhaar

Paul-Drude-Institut für Festkörperelektronik, Hausvogteiplatz 5-7, 10117 Berlin, Germany

Andreas Biermanns

University of Siegen, Solid State Physics, 57068 Siegen, Germany

Sondes Bauer

ANKA, Karlsruhe Institute of Technology, Hermann-von-Helmholtz-Platz 1, 76344 Eggenstein-Leopoldshafen, Germany

Sergey Lazarev

ANKA, Karlsruhe Institute of Technology, Hermann-von-Helmholtz-Platz 1, 76344 Eggenstein-Leopoldshafen,
Germany and Institute for Photon Science and Synchrotron Radiation, Karlsruhe Institute of Technology,
Hermann-von-Helmholtz-Platz 1, 76344 Eggenstein-Leopoldshafen, Germany

Ullrich Pietsch

University of Siegen, Solid State Physics, 57068 Siegen, Germany

Tilo Baumbach[*]

ANKA, Karlsruhe Institute of Technology, Hermann-von-Helmholtz-Platz 1, 76344 Eggenstein-Leopoldshafen, Germany;
Institute for Photon Science and Synchrotron Radiation, Karlsruhe Institute of Technology,
Hermann-von-Helmholtz-Platz 1, 76344 Eggenstein-Leopoldshafen, Germany;
and Laboratory for Application of Synchrotron Radiation, Karlsruhe Institute of Technology,
Kaiserstraße 12, 76131 Karlsruhe, Germany

In III-V nanowires the energetic barriers for nucleation in the zinc blende or wurtzite arrangement are typically of a similar order of magnitude. As a result, both arrangements can occur in a single wire. Here, we investigate the evolution of this polytypism in self-catalyzed GaAs nanowires on Si(111) grown by molecular beam epitaxy with time-resolved *in situ* x-ray diffraction. We interpret our data in the framework of a height dependent Markov model for the stacking in the nanowires. In this way, we extract the mean sizes of faultless wurtzite and zinc blende segments—a key parameter of polytypic nanowires—and their temporal evolution during growth. Thereby, we infer quantitative information on the differences of the nucleation barriers including their evolution without requiring a model of the nucleus.

Semiconductor nanowires (NWs) offer a variety of capabilities for applications [1,2] such as transistors [3,4], lasing [5,6], solar cells [7], thermoelectric materials [8], and sensors [9,10] as well as for fundamental research, e.g., on qubits [11], single photon sources [12], or Majorana fermions [13]. In most cases, NWs with a minimum of defects such as impurity atoms, dislocations (and the induced strain thereof), and stacking faults are required. Although lateral strain relaxation in a NW facilitates a strongly reduced dislocation density compared

to conventional 2D layer growth in lattice-mismatched heteroepitaxy [14–16], the wurtzite zinc blende polytypism [17] deteriorates electronic and optical properties of III/V NWs [18–20]. This polytypism refers to the observation that wurtzite (WZ) and zinc blende (ZB) phase can coexist in a single NW [21], although typically only one phase is stable in the bulk material.

Growing a NW often involves a liquid droplet at its tip which induces uniaxial growth and serves as a material reservoir during the growth process [22]. The properties of

the droplet during the growth—such as its shape, composition, and dynamics [23–26]—have a strong impact on the growing NW. Further, the morphology [27–29] of the growing NW, the involved crystallographic surfaces, and their energies [30,31] are of importance, in particular for the currently growing phase. As a result, a complicated interplay of the crystalline wire and the droplet determines the energetic nucleation barriers $E_{P|P}$ and $E_{\bar{P}|P}$ for continuing the growth of phase $P \in \{ZB, WZ\}$ or for beginning a segment of the complementary phase $\bar{P}$ on top of the current phase P [30,32–34]. The nucleation barrier differences $\delta E_{\bar{P}|P} = E_{\bar{P}|P} - E_{P|P}$ determine the polytypic behavior: If $\delta E_{\bar{P}|P}$ significantly exceed the energy scale $k_B T_{\mathrm{growth}}$ responsible for thermal fluctuations (k_B is the Boltzmann constant and T_{growth} the growth temperature in Kelvin), phase transitions are highly unlikely and very pure wires emerge. In contrast, the frequent observation of polytypism implies that $\delta E_{\bar{P}|P}$ is only slightly larger than $k_B T_{\mathrm{growth}}$ for typical growth conditions. Moreover, experimental access to that quantity is of crucial importance for phase engineering in NWs. Consequently, considerable theoretical [25,33,35–37] and experimental [32,38] efforts are aimed at understanding and controlling [17,27] polytypism.

As a result of the different lattice constants of the polytypes in NWs [39–42], x-ray diffraction is well suited for investigation of polytypism in NWs [43–46]. In this manuscript, we infer the differences of the nucleation barriers $\delta E_{\bar{P}|P}$ and the evolution thereof from time-resolved *in situ* x-ray diffraction data which have been obtained during growth of NWs. The changes in the shape of the scattered intensity over time (beyond simple rescaling due to increased scattering volume or effects from changes in the geometry of the NWs) reveal the gradient of the properties of the NWs with increasing growth time. For interpretation of the time-resolved experimental data, we employ a model for the length distribution of faultless segments of each polytype with a mean value L_P ("phase purity"). As an advantage of this approach, the derived nucleation barrier differences $\delta E_{\bar{P}|P}$ rely neither on assumptions on the geometry of the nucleus, nor on the exact mechanisms of nucleation or the catalyst dynamics [22,24,26,30,31,33–36,38,47].

We perform our measurements in a special molecular beam epitaxy (MBE) system [48] dedicated to time-resolved *in situ* x-ray diffraction (see Fig. 1 and [49]) at the NANO beam line of the synchrotron facility ANKA at KIT during the growth of self-catalyzed GaAs NWs on Si(111).

In addition to the time-resolved x-ray data of the (111) reflection of GaAs recorded during growth, a three dimensional postgrowth scan of this reflection in reciprocal space was performed *in situ* after the growth was stopped: Apart from the silicon Bragg peak, its diffuse scattering and
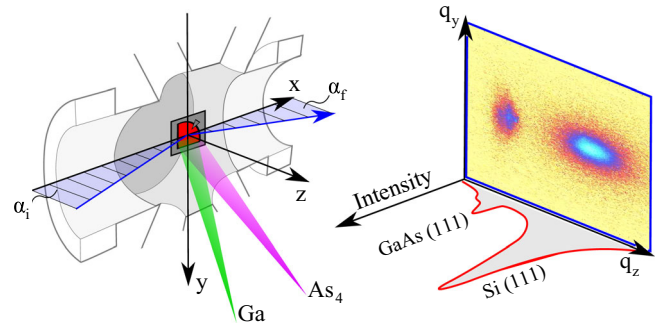
FIG. 1 (color online). Illustration of the experimental setup: MBE growth chamber with vertically mounted substrate (red). The x-ray beam hits the sample under the angle $\alpha_i \approx 8°$. The 2D detector frames (blue box) register the intensity scattered by $\alpha_i + \alpha_f \approx 16°$. The q_z axis indicates the momentum transfer parallel to the growth direction of the NWs. Integration in the q_y direction results in q_z profiles which contain diffuse scattering of the silicon substrate and a GaAs peak with a highly nontrivial shape.

the crystal truncation rod of the substrate, an extended diffuse cloud of intensity close to the GaAs Bragg peak is observed [49]. Additional postgrowth *ex situ* scanning electron microscopy (SEM) [49] reveals low-density NWs (around 2 NWs per μm^2) with approximately 17 ± 5 nm in diameter and a height of 2.2 ± 0.25 μm.

During growth, the arrangement of beam, sample, and detector has been kept constant. The information recorded by the 2D x-ray detector essentially corresponds to the q_y-q_z plane in reciprocal space as illustrated in the Supplemental Material [49]. The recorded frames have been corrected for background and integrated in the q_y direction [49]. Thereby we obtain time-resolved q_z profiles, which are sensitive to the arrangement of the crystalline layers in the NWs which are parallel to the (111) surface of the substrate.

Figure 2 contains these profiles $\mathcal{I}(q_z, t_i)$ after various growth times t_i (symbols). Although the external growth parameters have been kept constant during growth, we
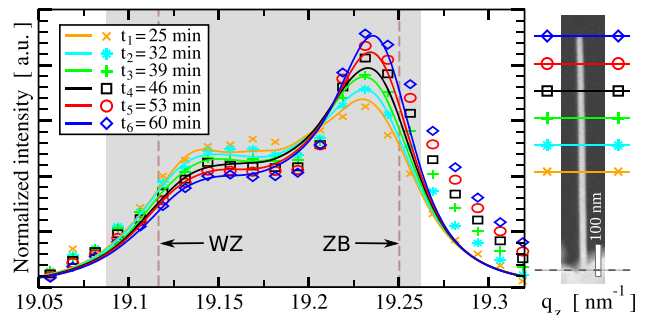
FIG. 2 (color online). Measured *in situ* x-ray diffraction intensity profiles $\mathcal{I}(q_z, t_i)$ after various growth times t_i (symbols) and the best fit of the simulated profiles based on Eq. (2) (solid lines) in the gray region. Each profile has been normalized to an equal area in the gray region.

observe a monotonic drift of the scattered intensity $\mathcal{I}(q_z, t_i)$ towards zinc blende (smaller vertical lattice constant [40,50]) with advancing growth time t_i which indicates a gradient of the properties of the NWs with increasing height.

We now relate these profiles of the scattered x-ray intensity to time-resolved information on the purities L_P of both phases and the differences $\delta E_{\bar{P}|P}$ of the nucleation barriers.

For that purpose, we generate stacking sequences of a large set of wires based on a time-dependent Markov chain—motivated, e.g., by the results in [32,37]. Then, we calculate the respective q_z profile of this set of NWs. Finally, we compare the set of profiles $\{\mathcal{I}(q_z, t_i)\}$ resulting from different parameters of the Markov chain to the experimentally measured intensity distribution. The solid lines in Fig. 2 correspond to our best fit in the framework of the time-dependent Markov model.

We now discuss this model in more detail. First, we relate the stacking sequence to the wurtzite and zinc blende phase: The vertical stacking of each wire is constituted by a sequence of layers of either type A, B or C. The zinc blende phase is composed of three adjacent layers of different types (e.g., ABC). In particular, the type of the first and last layer is different. The wurtzite phase is defined by three adjacent layers where the first and last layer are of the same type (e.g., ABA). Direct repetitions of the same type in the sequence (e.g., $ABBC$) are not allowed.

In our simulations, we initialize the first three layers of each wire in wurtzite stacking with probability $p_{\mathrm{WZ}}^{(0)}$ and, consequently, zinc blende with probability $1 - p_{\mathrm{WZ}}^{(0)}$. After this, we append a new layer n to the wire's stacking sequence according to a Markov chain: First, the current phase P is determined by a comparison of layer $n-1$ and $n-3$. Layer n continues the sequence of the current phase P with probability $p_{P \to P}(n)$ and switches to the stacking of the complementary phase $\bar{P}$ with probability $p_{P \to \bar{P}}(n) = 1 - p_{P \to P}(n)$. This Markov chain is repeated until n reaches the total number of layers n_l corresponding to a particular growth time ($n_l \approx 6700$ after $t_{\max} = 60$ min, equivalent to 2.1 μm in height). For growth times $t_{\max} < 60$ min, we assume a linear relation between the NW height n_l and the growth time t.

The parameters $p_{P \to \bar{P}}(n)$ in the stacking model determine the phase distribution of the grown wires. In the case of probabilities $p_{P \to \bar{P}}$ independent of the layer n the phase fractions for long wires (stationary limit for $n_l \to \infty$, [49]) are $p_P^{(S)} = p_{\bar{P} \to P}/(p_{\bar{P} \to P} + p_{P \to \bar{P}})$, and the thicknesses of the phase segments are exponentially distributed with mean $L_P = p_{P \to P}/p_{P \to \bar{P}}$. Such exponential behavior has, for example, been observed with high resolution transmission electron microscopy (HRTEM) by Johansson *et al.* [32,34] for values in the order of $L_P \approx 3$–9 layers.

However, the longer the mean phase segment, the large fluctuations of the thickness of each individual phase segment make the detection of the mean value L_P—and in particular a possible change along the wire—more and more difficult by means of HRTEM. On the contrary, the high statistical significance of x-ray ensemble measurements will facilitate the detection of a gradient in L_P in the growth direction of the NWs in a range that is currently not accessible by other methods and despite the huge fluctuations of the length of the phase segments.

Consequently, we now discuss the relation between the stacking sequences of the nanowires and the q_z profiles close to the (111) GaAs reflection. Then, we illustrate the influence of the phase fractions $p_P^{(S)}$ and purities L_P on such profiles for probabilities $p_{P \to \bar{P}}$ independent of the layer n
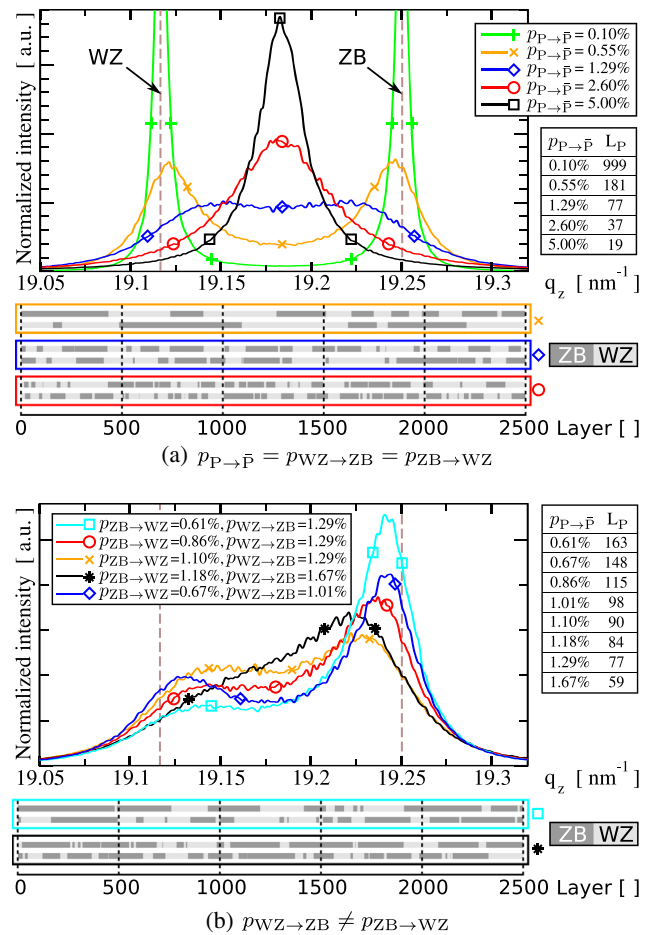
FIG. 3 (color online).   Intensity profiles near the (111) GaAs Bragg peak for ensembles of NWs with stacking sequences obtained by a Markov chain with layer independent transition probabilities $p_{P \to \bar{P}}$. The area below all profiles is equal. For some parameters (indicated by the color of the box enclosing the NW realizations), we added two examples for the phase distributions generated according to the Markov model. In (a), the parameters $p_{\mathrm{WZ} \to \mathrm{ZB}}$ and $p_{\mathrm{ZB} \to \mathrm{WZ}}$ are equal, whereas (b) illustrates the result for $p_{\mathrm{WZ} \to \mathrm{ZB}} \neq p_{\mathrm{ZB} \to \mathrm{WZ}}$.

(see Fig. 3). Finally, we introduce layer dependent transition probabilities $p_{P \to \bar{P}}(n)$ in order to understand the time-dependent experimental x-ray data.

A single NW contributes to the scattered intensity $\mathcal{I}(q_z)$ near the symmetric (111) Bragg reflection as the absolute square of the single wire scattering factor

$$\mathcal{F}(q_z, \mathbf{q}_\perp) \propto \sum_{n=1}^{n_l} \Omega_n(\mathbf{q}_\perp) \sum_{\substack{\alpha \in \\ \{Ga, As\}}} f_{\mathbf{Q}_B}^{(\alpha)} e^{-iq_z(z_n + z_{\alpha n})}, \quad (1)$$

where $f_{\mathbf{Q}_B}^{(\alpha)}$ is the atomic form factor of Ga and As atoms approximated by the value at the (111) Bragg peak $\mathbf{Q}_B$. z_n refers to the beginning of layer n and $z_{\alpha n}$ is the distance of the As sublayer to the Ga sublayer within the same layer n. $\Omega_n(\mathbf{q}_\perp)$ is the two-dimensional Fourier transform of the cross section of layer n. For our NWs we observe no pronounced tapering and, therefore, simplify $\Omega_n(\mathbf{q}_\perp) = \Omega(\mathbf{q}_\perp)$. However, geometrical information on tapering of NWs (e.g., from postgrowth SEM) can be incorporated easily through $\Omega_n(\mathbf{q}_\perp)$. The dependence of $\mathbf{q}_\perp$ is irrelevant for the subsequent discussions, as demonstrated in Ref. [49].

For the determination of z_n and $z_{\alpha n}$, we attribute the thickness of layer n according to the native value of the local phase (determined from layer $n-1$ and $n+1$ in the stacking sequence of this wire). For the ratio of the vertical lattice constants of the wurtzite and zinc blende polytypes, we employ $d_{WZ}/d_{ZB} = 1.007$ [40], where $d_P = z_n - z_{n-1}$. Finally, the contributions from 2500 different wires are summed up incoherently in our simulated data.

In Fig. 3 we depict simulated q_z intensity profiles close to the (111) GaAs Bragg reflection for layer independent transition probabilities $p_{P \to \bar{P}}$. These examples provide an overview of how the characteristic features of the x-ray profile change with either the phase fraction or with the phase purity at constant phase fraction and, thereby, facilitate a qualitative understanding of the experimental profiles in Fig. 2.

Although the fraction of wurtzite and zinc blende are equal to 50% in all curves of Fig. 3(a), the x-ray signal strongly differs in shape depending on the wires' phase purity: Starting from NWs with high phase purity (low transition probability), the diffraction signal shows sharp maxima at either the wurtzite or zinc blende position (dashed lines, respectively). For increasing transition probability, peak broadening is observed ($p_{P \to \bar{P}} \approx 0.55\%$) which results in a pronounced plateau at $p_{P \to \bar{P}} = 1.29\%$. For even higher transition probabilities ($p_{P \to \bar{P}} \in \{2.60\%, 5.00\%\}$), only a single peak centered at the mean q_z value of the pure wurtzite peak and the pure zinc blende peak remains. In Fig. 3(b), we consider an ensemble of wires with $p_P^{(S)} \neq 0.5$ which implies $p_{WZ \to ZB} \neq p_{ZB \to WZ}$. On the one hand, the three cases with $p_{WZ \to ZB} = 1.29\%$

illustrate the change in the x-ray signal as a function of the phase fraction $p_P^{(S)}$, where $p_P^{(S)}$ increases from $p_P^{(S)} = 0.32$ ($p_{ZB \to WZ} = 0.61\%$) over $p_P^{(S)} = 0.4$ ($p_{ZB \to WZ} = 0.86\%$) to $p_P^{(S)} = 0.46$ ($p_{ZB \to WZ} = 1.10\%$). On the other hand, the wurtzite fraction of the three cases $p_{ZB \to WZ} \in \{0.67\%, 0.86\%, 1.18\%\}$ is equal ($p_{WZ}^{(S)} = 0.4$). As well as for $p_P^{(S)} = 0.5$ in Fig. 3(a), the x-ray profile changes significantly as a function of the phase purities L_P for $p_P^{(S)} \neq 0.5$. Thus, the q_z intensity profile near the (111) Bragg reflection is highly sensitive to the transition probabilities and, thereby, reveals the average segment thickness of each polytype in the NW ensemble.

If no time-resolved experimental data are available, i.e., if only a single experimental profile $\mathcal{I}(q_z, t_i)$ after a particular time t_i in Fig. 2 is considered, it can be explained by *static* transition probabilities $p_{P \to \bar{P}}$ as its features are very similar to the profiles depicted in Fig. 3(b) (e.g., $p_{ZB \to WZ} = 1.10\%$ for $t_1 = 25$ min and $p_{ZB \to WZ} = 0.86\%$ for $t_5 = 53$ min). However, the change in the experimental profile with increasing growth time t_i is *incompatible* with static transition probabilities $p_{P \to \bar{P}}$. We attribute these changes to a nonvanishing gradient of the structural properties of the grown NWs with increasing height.

Thus, we consider layer dependent transition probabilities

$$p_{P \to \bar{P}}(n) = u_{P \to \bar{P}} + v_{P \to \bar{P}} \cdot n \quad (2)$$
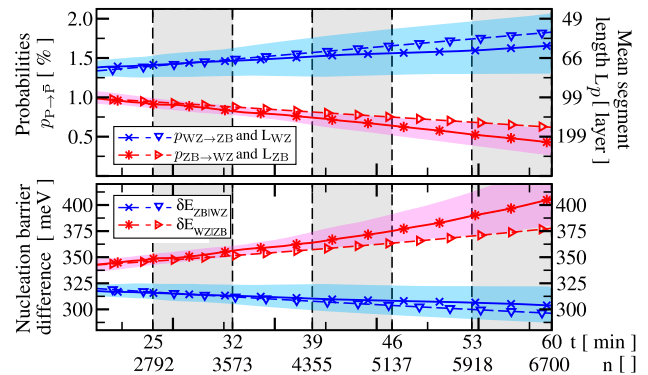
FIG. 4 (color online). Extracted transition probabilities $p_{P \to \bar{P}}(n)$ according to Eq. (2), mean segment lengths $L_P(n) \approx p_{P \to P}/p_{P \to \bar{P}}$ of newly grown segments (phase purity), and differences of the nucleation barriers $\delta E_{\bar{P}|P}(n)$ as given in Eq. (3) as a function of the layer n (or the growth time t). The triangular symbols represent the best fit of the simulated data to $\mathcal{I}(q_z, t_i)$ in the gray region in Fig. 2. The values depicted by cross, circle, and star symbols are the median at each layer n of the best $N_F = 60$ fits. The errors are estimated by the 25% and 75% quantiles thereof and marked as color shaded background. The negative (positive) slope in the case of $p_{ZB \to WZ}$ ($p_{WZ \to ZB}$) implies an increasing (decreasing) phase purity for zinc blende (wurtzite) with advancing time.

and generated a data base of intensity profiles $\mathcal{I}(q_z, t_i)$ for $N = 6000$ sets of random parameters $u_{P \to \bar{P}}$ and $v_{P \to \bar{P}}$ [49].

From the comparison to the experimental data, we obtain estimates for the layer dependent transition probabilities $p_{P \to \bar{P}}(n)$ which are depicted in Fig. 4: Whereas newly grown zinc blende and wurtzite segments are approximately equally thick (with $L_P \approx 80$) at early growth times $t \approx 20$ min, the average segment thickness of zinc blende $L_{ZB} \approx 200$ becomes about 3.5 times larger than the one of wurtzite after $t_{max} = 60$ min.

Finally, we exploit the probabilities $p_{P \to \bar{P}}(n)$ for making conclusions on the differences of the nucleation barriers [33,34,49]

$$\delta E_{\bar{P}|P}(n) = k_B T_{sub} \ln \left(\frac{1 - p_{P \to \bar{P}}(n)}{p_{P \to \bar{P}}(n)} \right), \qquad (3)$$

which are also depicted in Fig. 4 for our particular growth conditions. We obtain values [49] in the range from 315 meV (after $t \approx 25$ min) to 300 meV (after $t_{max} = 60$ min) for $\delta E_{ZB|WZ}(n)$. For $\delta E_{WZ|ZB}(n)$, we extracted 350 meV (after $t \approx 25$ min) to approximately 400 meV (after $t_{max} = 60$ min).

In contrast to experiments with varying growth conditions [43], we observe a trend towards higher phase purity of zinc blende despite constant growth parameters [49]. This behavior can be attributed to the dynamics of the droplet at the NW tip, in particular its shape and its composition. First, the supersaturation of As in the liquid droplet might increase during growth, which would lead to a higher probability for the nucleation of zinc blende [51]. Second, the volume of the liquid droplet, which is mainly constituted by Ga, might decrease [36]. This could result from a reduction in the Ga flux towards the droplet via the NW side walls as the NW grows longer [52–54]. Since there is no evidence for an onset of pronounced tapering [55] (which would indicate a reduction of the diameter of the droplet), the reduced volume likely induces a decrease of the wetting angle of the droplet rather than a reduction of its diameter [36].

In conclusion, we demonstrated that the temporal evolution of the intensity $\mathcal{I}(q_z, t)$ obtained by *in situ* x-ray diffraction provides quantitative access to the nucleation barrier differences which determine the phase distribution of the grown NWs. Based on a layer-dependent Markov chain in order to model polytypism, height dependent estimates for the phase purity for the ensemble of NWs have been extracted. For our particular growth conditions, a gradient of the phase purity towards larger zinc blende segments has been observed with advancing growth time. From the transition probabilities $p_{P \to \bar{P}}(n)$ in the Markov model we inferred layer-dependent differences of the nucleation barriers $\delta E_{\bar{P}|P}(n)$. For our example of self-catalyzed GaAs NWs, the values of $\delta E_{\bar{P}|P}(n)$ evolved in the range from 300 to 400 meV. We emphasize that the determined values rely neither on a particular geometrical model for the nucleus, nor on the exact mechanisms of nucleation or the catalyst dynamics.

Providing such access to the nucleation energy barriers, our approach opens a way for systematic studies of the evolution of polytypism during the growth of NWs. Thus, we are confident that the approach will gain great importance for further understanding and developing of theoretical and practical aspects of NW growth.

---

*tilo.baumbach@kit.edu

[1] O. Hayden, R. Agarwal, and W. Lu, Nano Today **3**, 12 (2008).

[2] K. Tomioka, T. Tanaka, S. Hara, K. Hiruma, and T. Fukui, IEEE J. Sel. Top. Quantum Electron. **17**, 1112 (2011).

[3] J. Xiang, W. Lu, Y. Hu, Y. Wu, H. Yan, and C. M. Lieber, Nature (London) **441**, 489 (2006).

[4] K. Tomioka, M. Yoshimura, and T. Fukui, Nature (London) **488**, 189 (2012).

[5] X. Duan, Y. Huang, R. Agarwal, and C. M. Lieber, Nature (London) **421**, 241 (2003).

[6] D. Saxena, S. Mokkapati, P. Parkinson, N. Jiang, Q. Gao, H. H. Tan, and C. Jagadish, Nat. Photonics **7**, 963 (2013).

[7] B. Tian, X. Zheng, T. J. Kempa, Y. Fang, N. Yu, G. Yu, J. Huang, and C. M. Lieber, Nature (London) **449**, 885 (2007).

[8] A. I. Hochbaum, R. Chen, R. D. Delgado, W. Liang, E. C. Garnett, M. Najarian, A. Majumdar, and P. Yang, Nature (London) **451**, 163 (2008).

[9] Y. Cui, Q. Wei, H. Park, and C. M. Lieber, Science **293**, 1289 (2001).

[10] E. Stern, J. F. Klemic, D. A. Routenberg, P. N. Wyrembak, D. B. Turner-Evans, A. D. Hamilton, D. A. LaVan, T. M. Fahmy, and M. A. Reed, Nature (London) **445**, 519 (2007).

[11] J. Cartwright, Nat. News, doi:10.1038/news.2010.694 (2010).

[12] M. E. Reimer, G. Bulgarini, N. Akopian, M. Hocevar, M. B. Bavinck, M. A. Verheijen, E. P. A. M. Bakkers, L. P. Kouwenhoven, and V. Zwiller, Nat. Commun. **3**, 737 (2012).

[13] V. Mourik, K. Zuo, S. M. Frolov, S. R. Plissard, E. P. A. M. Bakkers, and L. P. Kouwenhoven, Science **336**, 1003 (2012).

[14] F. Glas, Phys. Rev. B **74**, 121302 (2006).

[15] K. L. Kavanagh, Semicond. Sci. Technol. **25**, 024006 (2010).

[16] X. Zhang, V. G. Dubrovskii, N. V. Sibirev, and X. Ren, Cryst. Growth Des. **11**, 5441 (2011).

[17] K. A. Dick, P. Caroff, J. Bolinsson, M. E. Messing, J. Johansson, K. Deppert, L. R. Wallenberg, and L. Samuelson, Semicond. Sci. Technol. **25**, 024009 (2010).

[18] J. Bao, D. C. Bell, F. Capasso, J. B. Wagner, T. Mårtensson, J. Trägårdh, and L. Samuelson, Nano Lett. **8**, 836 (2008).

[19] D. Spirkoska, J. Arbiol, A. Gustafsson, S. Conesa-Boj, F. Glas, I. Zardo, M. Heigoldt, M. H. Gass, A. L. Bleloch, S. Estrade, M. Kaniber, J. Rossler, F. Peiro, J. R. Morante, G. Abstreiter, L. Samuelson, and A. Fontcuberta i Morral, Phys. Rev. B **80**, 245325 (2009).

[20] M. Hjort, S. Lehmann, J. Knutsson, R. Timm, D. Jacobsson, E. Lundgren, K. Dick, and A. Mikkelsen, Nano Lett. **13**, 4492 (2013).

[21] M. Koguchi, H. Kakibayashi, M. Yazawa, K. Hiruma, and T. Katsuyama, Jpn. J. Appl. Phys. **31**, 2061 (1992).

[22] R. S. Wagner and W. C. Ellis, Appl. Phys. Lett. **4**, 89 (1964).

[23] M. Moseler, F. Cervantes-Sodi, S. Hofmann, G. Csányi, and A. C. Ferrari, ACS Nano **4**, 7587 (2010).

[24] A. D. Gamalski, C. Ducati, and S. Hofmann, J. Phys. Chem. C **115**, 4413 (2011).

[25] V. G. Dubrovskii, G. E. Cirlin, N. V. Sibirev, F. Jabeen, J. C. Harmand, and P. Werner, Nano Lett. **11**, 1247 (2011).

[26] A. D. Gamalski, J. Tersoff, R. Sharma, C. Ducati, and S. Hofmann, Phys. Rev. Lett. **108**, 255702 (2012).

[27] P. Caroff, K. A. Dick, J. Johansson, M. E. Messing, K. Deppert, and L. Samuelson, Nat. Nanotechnol. **4**, 50 (2009).

[28] J. Johansson, K. A. Dick, P. Caroff, M. E. Messing, J. Bolinsson, K. Deppert, and L. Samuelson, J. Phys. Chem. C **114**, 3837 (2010).

[29] C.-Y. Wen, J. Tersoff, K. Hillerich, M. C. Reuter, J. H. Park, S. Kodambaka, E. A. Stach, and F. M. Ross, Phys. Rev. Lett. **107**, 025503 (2011).

[30] R. E. Algra, M. A. Verheijen, M. T. Borgström, L.-F. Feiner, G. Immink, W. J. P. van Enckevort, E. Vlieg, and E. P. A. M. Bakkers, Nature (London) **456**, 369 (2008).

[31] H. J. Joyce, J. Wong-Leung, Q. Gao, H. H. Tan, and C. Jagadish, Nano Lett. **10**, 908 (2010).

[32] J. Johansson, L. S. Karlsson, C. Patrik T. Svensson, T. Mårtensson, B. A. Wacaser, K. Deppert, L. Samuelson, and W. Seifert, Nat. Mater. **5**, 574 (2006).

[33] F. Glas, J.-C. Harmand, and G. Patriarche, Phys. Rev. Lett. **99**, 146101 (2007).

[34] J. Johansson, L. S. Karlsson, K. A. Dick, J. Bolinsson, B. A. Wacaser, K. Deppert, and L. Samuelson, Cryst. Growth Des. **9**, 766 (2009).

[35] V. G. Dubrovskii, N. V. Sibirev, J. C. Harmand, and F. Glas, Phys. Rev. B **78**, 235301 (2008).

[36] P. Krogstrup, S. Curiotto, E. Johnson, M. Aagesen, J. Nygård, and D. Chatain, Phys. Rev. Lett. **106**, 125505 (2011).

[37] J. Johansson, J. Bolinsson, M. Ek, P. Caroff, and K. A. Dick, ACS Nano **6**, 6142 (2012).

[38] P. Caroff, J. Bolinsson, and J. Johansson, IEEE J. Sel. Top. Quantum Electron. **17**, 829 (2011).

[39] C.-Y. Yeh, Z. W. Lu, S. Froyen, and A. Zunger, Phys. Rev. B **46**, 10086 (1992).

[40] A. Biermanns, S. Breuer, A. Davydok, L. Geelhaar, and U. Pietsch, Phys. Status Solidi RRL **5**, 156 (2011).

[41] D. Kriegner, C. Panse, B. Mandl, K. A. Dick, M. Keplinger, J. M. Persson, P. Caroff, D. Ercolani, L. Sorba, F. Bechstedt, J. Stangl, and G. Bauer, Nano Lett. **11**, 1483 (2011).

[42] C. Panse, D. Kriegner, and F. Bechstedt, Phys. Rev. B **84**, 075217 (2011).

[43] P. Krogstrup, M. Hannibal Madsen, W. Hu, M. Kozu, Y. Nakata, J. Nygård, M. Takahasi, and R. Feidenhans'l, Appl. Phys. Lett. **100**, 093103 (2012).

[44] D. Kriegner, J. M. Persson, T. Etzelstorfer, D. Jacobsson, J. Wallentin, J. B. Wagner, K. Deppert, M. T. Borgström, and J. Stangl, Thin Solid Films **543**, 100 (2013).

[45] S. T. Haag, M.-I. Richard, V. Favre-Nicolin, U. Welzel, L. P. H. Jeurgens, S. Ravy, G. Richter, E. J. Mittemeijer, and O. Thomas, Thin Solid Films **530**, 113 (2013).

[46] J. Gulden, S. O. Mariager, A. P. Mancuso, O. M. Yefanov, J. Baltser, P. Krogstrup, J. Patommel, M. Burghammer, R. Feidenhans'l, and I. A. Vartanyants, Phys. Status Solidi A **208**, 2495 (2011).

[47] F. Glas, M. R. Ramdani, G. Patriarche, and J.-C. Harmand, Phys. Rev. B **88**, 195304 (2013).

[48] T. Slobodskyy, P. Schroth, D. Grigoriev, A. A. Minkevich, D. Z. Hu, D. M. Schaadt, and T. Baumbach, Rev. Sci. Instrum. **83**, 105112 (2012).

[49] See Supplemental Material at http://link.aps.org/supplemental/10.1103/PhysRevLett.114.055504 for details on the experiment, Markov model, and data processing and evaluation, which includes Refs. [50,56–59].

[50] M. Köhl, P. Schroth, A. A. Minkevich, J.-W. Hornung, E. Dimakis, C. Somaschini, L. Geelhaar, T. Aschenbrenner, S. Lazarev, D. Grigoriev, U. Pietsch, and T. Baumbach, J. Synchrotron Radiat. **22**, 67 (2015).

[51] M. Yamaguchi, J.-H. Paek, and H. Amano, Nanoscale Res. Lett. **7**, 558 (2012).

[52] V. G. Dubrovskii, N. V. Sibirev, G. E. Cirlin, J. C. Harmand, and V. M. Ustinov, Phys. Rev. E **73**, 021603 (2006).

[53] C. Colombo, D. Spirkoska, M. Frimmer, G. Abstreiter, and A. Fontcuberta i Morral, Phys. Rev. B **77**, 155326 (2008).

[54] V. Pankoke, S. Sakong, and P. Kratzer, Phys. Rev. B **86**, 085425 (2012).

[55] J. C. Harmand, G. Patriarche, N. Péré-Laperne, M.-N. Mérat-Combes, L. Travers, and F. Glas, Appl. Phys. Lett. **87**, 203101 (2005).

[56] A. Biermanns, S. Breuer, A. Trampert, A. Davydok, L. Geelhaar, and U. Pietsch, Nanotechnology **23**, 305703 (2012).

[57] A. Davydok, S. Breuer, A. Biermanns, L. Geelhaar, and U. Pietsch, Nanoscale Res. Lett. **7**, 109 (2012).

[58] A. Biermanns, S. Breuer, A. Davydok, L. Geelhaar, and U. Pietsch, J. Appl. Crystallogr. **45**, 239 (2012).

[59] M. W. Larsson, J. B. Wagner, M. Wallin, P. Håkansson, L. E. Fröberg, L. Samuelson, and L. R. Wallenberg, Nanotechnology **18**, 015504 (2007).